Developments for resonance ionization laser spectroscopy of the heaviest elements at SHIP[☆]

F. Lautenschläger[a,1], P. Chhetri[a,b], D. Ackermann[b], H. Backe[d], M. Block[b,c,d], B. Cheal[g], A. Clark[b], C. Droese[e,b], R. Ferrer[h], F. Giacoppo[b,c], S. Götz[b,c], F.P. Heßberger[b,c], O. Kaleja[a], J. Khuyagbaatar[b,c], P. Kunz[f], A. K. Mistry[b,c], M. Laatiaoui[b,c], W. Lauth[d], S. Raeder[b,c,*], Th. Walther[a], C. Wraith[g]

[a]*Technische Universität Darmstadt, Schloßgartenstraße 7, 64289 Darmstadt, Germany*
[b]*GSI Helmholtzzentrum für Schwerionenforschung, Planckstraße 1, 64291 Darmstadt, Germany*
[c]*Helmholtz Institut Mainz, Johann-Joachim-Becherweg 36, 55128 Mainz, Germany*
[d]*Johannes Gutenberg Universität Mainz, Johann-Joachim-Becher-Weg 45, 55128 Mainz, Germany*
[e]*Ernst Moritz Arndt Universität Greifswald, Domstraße 11, 17487 Greifswald, Germany*
[f]*TRIUMF, 4004 Wesbrook Mall, Vancouver BC, V6T 2A3, Canada*
[g]*University of Liverpool, Liverpool L69 3BX, United Kingdom*
[h]*KU Leuven, B-3001 Leuven, Belgium*

Abstract

The experimental determination of atomic levels and the first ionization potential of the heaviest elements ($Z \geq 100$) is key to challenge theoretical predictions and to reveal changes in the atomic shell structure. These elements are only artificially produced in complete-fusion evaporation reactions at on-line facilities such as the GSI in Darmstadt at a rate of, at most, a few atoms per second. Hence, highly sensitive spectroscopic methods are required. Laser spectroscopy is one of the most powerful and valuable tools to investigate atomic properties. In combination with a buffer-gas filled stopping cell, the Radiation Detected Resonance Ionization Spectroscopy (RADRIS) technique provides the highest sensitivity for laser spectroscopy on the heaviest elements. The RADRIS setup, as well as the measurement procedure, have been optimized and characterized using the α-emitter ^{155}Yb in on-line conditions, resulting in an overall efficiency well above 1%. This paves the way for a successful search of excited atomic levels in nobelium and heavier elements.

Keywords: Resonance ionization spectroscopy, gas stopping cell, Radiation Detected Resonance Ionization Spectroscopy, ytterbium, nobelium

1. Introduction

The study of the atomic structure of the elements with $Z \geq 100$ is one of the most fascinating and challenging disciplines of modern atomic physics, for an overview see [1]. For these elements, theoretical calculations indicate that relativistic effects alter the electron configuration and thus the atomic properties. In the heaviest actinide and trans-actinide elements the 5*f*-, 6*d*-, 7*s*-, and 7*p*- valence orbitals are occupied. Relativistic effects manifest in a shrinking of the $s-$ and $p_{1/2}-$ electron wave functions and a change in the nuclear potential screening by the inner shell electrons. This changes the binding energies of the valence electrons and influences the chemical properties of these elements. Hence, the measurement of atomic level energies, optical transitions as well as the first ionization potential (IP) of such elements provides a benchmark for modern atomic theories, for example multi-configuration Dirac-Fock (MCDF) and relativistic coupled-cluster (RCC) calculations [2]. At present, the most advanced experimental methods to investigate atomic properties of the heaviest elements are based on liquid- and gas-phase chemistry [3, 4]. Recently, a determination of the first IP of Lr ($Z = 103$) based on surface ionization was reported [5]. So far, fermium ($Z = 100$) is the heaviest element for which a direct identification of atomic levels was performed. This was done using laser spectroscopy in a buffer-gas cell in combination with ion detection [6]. However, the application to heavier elements is hampered by low

---

production rates of only a few atoms per second or less, calling for very sensitive experimental methods. For short-lived radionuclides, the RAdiation Detected Resonance Ionization Spectroscopy (RADRIS) [1, 7] technique provides the required sensitivity as demonstrated in the spectroscopy of the ^{240f,242f,244f}Am fission isomers [8]. Preparatory studies for extending the applicability of the technique to the element nobelium ($Z = 102$) were successfully conducted and resulted in a measurement of the desorption enthalpy of nobelium from tantalum and a first attempt on the search of atomic levels [9, 10]. In nobelium, a relatively simple atomic structure is expected according to various theoretical calculations which predict low lying and optically accessible atomic levels. In particular, a strong transition from the ground state is expected in the range of 28 500–30 100 cm^{-1}[11, 12, 13, 14]. Unfortunately the large uncertainties of these predictions pose an additional challenge for the application of laser spectroscopic techniques. The RADRIS setup, now permanently located at GSI, has been progressively improved for the laser spectroscopic studies of nobelium using the chemical homologue ytterbium through off- and on-line measurements. For on-line measurements the gas cell is placed behind the velocity filter SHIP which separates the recoil nuclei from the primary beam by using a combination of electric and magnetic fields [15]. The isotope ^{254}No (T$_{1/2}$ =51.2 s)[16] has a production cross section of 2 μb in the fusion-evaporation reaction ^{208}Pb(^{48}Ca, 2n)^{254}No at primary beam energy of approximately 4.55 A·MeV/u [17]. Considering available beam intensities and the transmission of the velocity filter SHIP, about four ^{254}No ions per seconds can be delivered to the gas cell. The setup can be tested using ytterbium, the homologue lanthanide of the actinide nobelium. The α-emitter ^{155}Yb can be produced via the fusion-evaporation reaction ^{112}Sn(^{48}Ca,5n)^{155}Yb with a cross section of 7.5 mb at a projectile energy of 4.55 A·MeV/u as calculated using the HIVAP code [18]. In this article, the characterization of an optimized setup is reported, including the buffer-gas cell, the data acquisition system (DAQ), the laser system, and laser radiation transport, as well as the measurement procedure. The performance in on-line experiments using ^{155}Yb, the expected performance for ^{254}No, and the best experimental conditions for the level search are addressed.

2. Experimental setup

The main component of the RADRIS setup is a buffer-gas filled stopping cell equipped with a catcher filament and two Passivated Implanted Planar Silicon
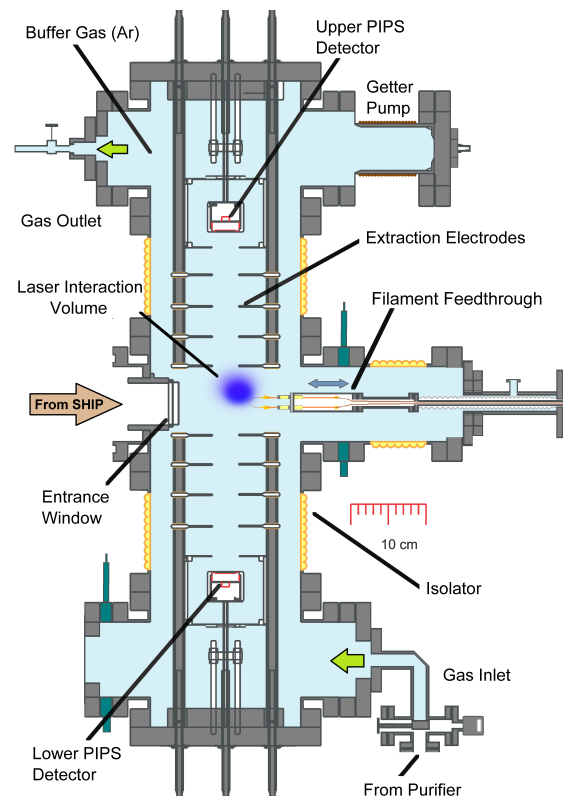

Figure 1: Schematic overview of the RADRIS gas cell showing the main parts in a lateral cut along the vertical plane.~~Schematic overview of the RADRIS gas cell.~~ For details see text.

(PIPS) detectors(see Fig.1). Inside the gas cell, the highly energetic recoils are stopped in 50–100 mbar high-purity argon gas. The thermalized ions are then guided by suitable electric potentials onto a thin tantalum catcher filament of 125 μm thickness where they are neutralized. After a half-life dependent accumulation time [19], the filament is heated for about 0.3 s to re-evaporate the captured neutral atoms from the filament. To allow for a detection of laser induced ions after this re-evaporation, the recoils from SHIP are only provided during the accumulation time. The evaporated atoms interact with the laser radiation sent into the gas cell and resonant ionization spectroscopy (RIS) can be carried out by applying a two step ionization scheme [20]. In off-line measurements the position of the laser beams with respect to the tip of the filament was optimized experimentally to be located about 2 cm higher and 1–2 cm towards the entrance window, which accounts for convection and diffusion in the pulse heated buffer gas. If the laser radiation is resonant
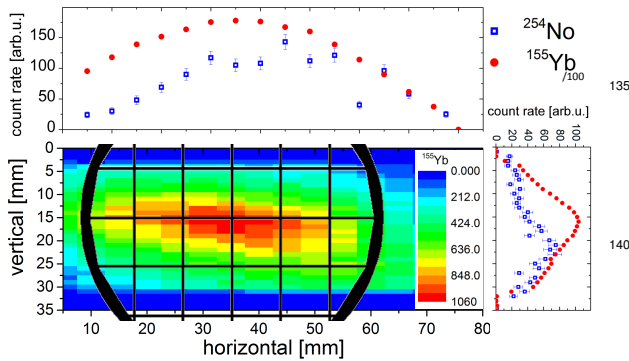
Figure 2: Spatial distribution of ^{155}Yb in front of the gas cell based on the registered alpha decays on a 16-strip silicon detector. The graphs on the top and the right side show the projections for ^{155}Yb and ^{254}No.

with an optical transition, the neutral atoms are excited and subsequently ionized to the continuum by high power radiation of a second laser. The photo ions are then guided by electrostatic potentials towards the PIPS detector for identification by their characteristic α-decay energy.

2.1. Gas Cell

The buffer-gas cell consists of three standard CF cross-pieces. The middle six-way cross hosts the entrance window and the catcher filament as well as two quartz windows for laser access. It is electrically isolated and can be set to voltages of at least 1200 V. The two four-way crosses are arranged symmetrically and contain an electrode system and an α-detector each. During the measurements, only one detector is used. The redundant copy guarantees a continuous operation in the event of a failure of the first detector. Between SHIP and the gas cell a vacuum chamber is located (not shown in Fig. 1) hosting three thin mylar degrader foils with different thicknesses to reduce the kinetic energy of the evaporation residues such that they can be subsequently stopped in the buffer-gas cell. A retractable α-detector unit is used to determine the incoming recoil rate as well as the recoil beam position and shape (*cf.* Fig. 2). The setup was optimized for maximum efficiency and a stable long-term operation.

Entrance window

The entrance window separates the gas cell stopping volume from the vacuum of the recoil separator SHIP. The window consists of a 3.5 µm-thick aluminum-coated mylar foil supported by a 1 mm thick stainless steel grid made of thin wires (0.5 mm thick) with a spacing of 9 mm on the vacuum side. To seal the entrance window a Viton O-ring is used. The holding structure of the window is designed to minimize perturbations of the electric potentials in the stopping volume. The window has a diameter of 56 mm and matches the incoming recoil beam size of about 50x22 mm^2 (FWHM) for ^{155}Yb. The measured distribution for ytterbium recoils is shown in Fig. 2 together with a sketch of the entrance window including the support grid.

Gas handling

Impurities in the buffer gas may result in efficiency losses due to neutralization from charge exchange processes and molecule formation, e.g., with oxygen or hydrogen. Prior to on-line application the system is therefore heated up to 90–100°C under high vacuum conditions. Using a turbomolecular pump and an ion getter pump (C-100 MK5, SAES) to efficiently remove evaporated impurities, pressures down to $2 \cdot 10^{-8}$ mbar are reached. After closing the gate valve to the vacuum pumps, Ar buffer gas with a purity level of 99.9999% is supplied. To reduce the impurities to the ppb level, the Ar gas additionally passes a getter-based purifier before entering the gas cell, as indicated by the green arrow in Fig. 1. The pressure is regulated by a mass-flow controller in conjunction with a capacitron pressure gauge for longterm operation. At the upper detector a needle valve is placed to enable a small continuous gas flow of $5 \cdot 10^{-2}$ mbar l s^{-1}. The gas purity is monitored by a Residual-Gas-Analyzer (RGA) equipped with a turbomulecular pump and connected to the buffer-gas cell via a needle valve to limit the pressure inside the RGA recipient to below 10^{-5} mbar. The partial pressures of residual impurities, especially of hydrogen and oxygen, were monitored during the on-line measurements.

Filament feedthrough

The filament assembly was optimized to ensure a well defined collection of the thermalized ions onto the tip of the filament in accord with ion-trajectory simulations using SIMION [21]. The leads of the filament were placed on an electrically isolated holding structure as shown in Fig.3. The holding structure is maintained at the same potential as the central cross-piece, minimizing field distortions. The filament current supply is galvanically isolated and can be biased up to 1100 V. The filament, a 125 µm thick Ta wire in the shape of a hyperbola, is crimped with copper tubes to the current leads made of silver-plated copper.
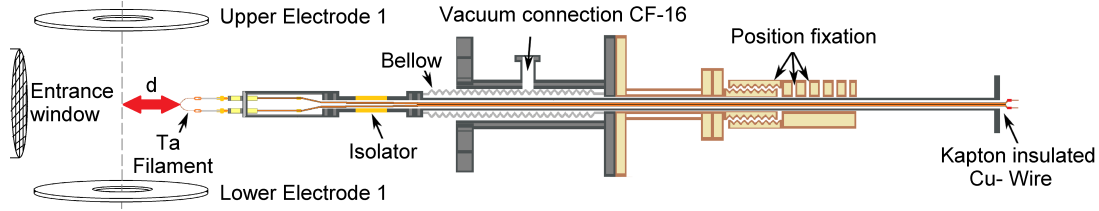
3

Figure 3: Schematic view of the central part of the cell with the filament feedthrough placed relative to the first electrodes and the entrance window. Modifications include the filament isolator which keeps the tantalum filament permanently on a high potential while the grafter itself is grounded for safety purposes.
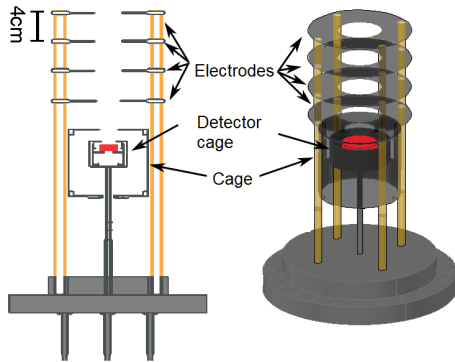

Figure 4: The combined electrode and detector system. All pieces are fixed by ceramic tubes, which are directly connected to the flange.

Table 1: Positive voltage ~~Voltage~~ settings for the two different configurations of collection onto the filament and guiding to one of the detectors. The detector setup with the corresponding labels is depicted in Fig. 4. The voltages applied to the electrodes 2–4 and the cage of the redundant arm are on the same potential as the corresponding electrodes in use.

Configuration	Capture	To detector
Filament	300 V	1015 V
Cross piece	746 V	1025 V
Opposing electrode 1	746 V	1025 V
Electrode 1	749 V	1000 V
Electrode 2	800 V	800 V
Electrode 3	605 V	605 V
Electrode 4	580 V	580 V
Cage	245 V	245 V
Detector cage	0 V	0 V

The linear feedthrough allows the location of the filament to be varied between a position located in the symmetry axis of the extraction electrode system and a full retraction. By using a gate valve, the filament can be exchanged without venting the gas cell. This is important if the filament breaks or ages, causing a decrease in efficiency.

Electrode and detector system

In the chamber, a set of ring-shaped electrodes is placed between the ionization region and each of the PIPS detectors. Each of the mirrored systems consists of four electrodes and a set of two metal cages enclosing the PIPS detectors as depicted in Fig. 4. The first three electrodes have an inner diameter of 44 mm, while the following electrode has an inner diameter of 36 mm. A fifth electrode is part of an outer cage to shield the detector from perturbing fields and has an inner diameter of 32 mm. In order to efficiently isolate them from each other, they are mounted on four ceramic tubes and the electrical connection is made with Kapton-insulated copper wires. The smallest spacing between two electrodes of 22 mm is between

the fourth electrode and the cage. The active area of the PIPS detector has a diameter of 27.6 mm and is placed in a small, grounded, cylindrical-shaped detector cage. The detector cage has an aperture of 30 mm, on top of which a 200 nm thick Kapton foil is placed, which is aluminized on the side towards the gas cell. Without a protecting foil, the infrared photons from the heated filament induce pile-up events in the detector signal. The foil additionally protects the detector from radioactive contamination and prevents electrical overload due to the filament heat pulse. The ion transmission through the electrode system towards the detector amounts to $\epsilon_{electrodes}$=100% according to SIMION simulations. Owing to the protection foil, the covered solid angle of the PIPS-detector is ϵ_{solid}=40%. The potentials of the electrodes were set depending on the measurement mode and typical parameters are given in Tab. 1. While collecting onto the filament
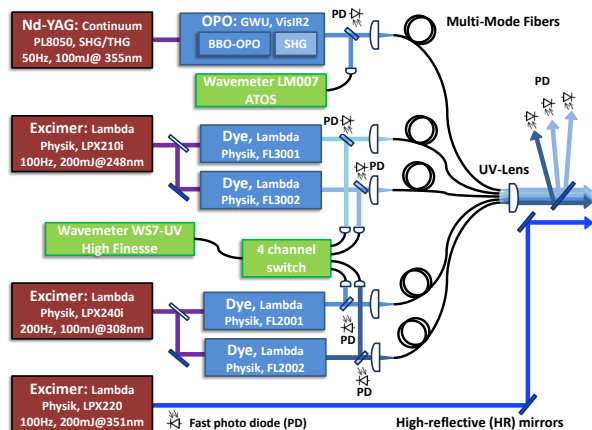
Figure 5: Schematic diagram of the laser system for the search of atomic levels. The beam transport to the experiment is indicated using optical multi mode fibers for the tunable lasers and 2 inch HR mirrors for the high intense laser pulses of the LPX220 excimer laser. The monitoring equipment for wavelength, timing and pulse energies using wavemeters and fast photodiodes is also sketched.

wire, the first two electrodes on each side were set to a high positive electric potential, guiding the ions onto the tip of the filament wire. During evaporation and laser irradiation, the potentials of the electrodes next to the detector in use were set for guiding ions towards the detector, while the opposing first electrode kept its repelling potential. This potential configuration was also applied to quantify the total number of stopped ions in the gas cell without catching them onto the filament.

2.2. Laser system and laser radiation transport

~~F~~The laser system employed ~~f~~or the search of atomic levels in the heaviest elements ~~consists~~ of four tunable dye lasers (Lambda Physik FL series) and an Optical Parametric Oscillator (OPO) system (GWU-Lasertechnik, VisIR2). The schematic layout is depicted in Fig.5. Two excimer laser (Lambda Physik, LPX2xxi series) are used to each pump two dye lasers. To cover a wide range of possible emission wavelengths, one of the excimer lasers (LPX210i) is operated with a Kr:F gas mixture with an emission wavelength of 248 nm, which enables pumping dyes emitting laser light in the ultraviolet (UV) regime between 311 and 352 nm as discussed in [19]. The second excimer laser (LPX240i) is operated with a Xe:Cl gas mixture resulting in an emission wavelength of 308 nm, with which dyes starting from 350 nm
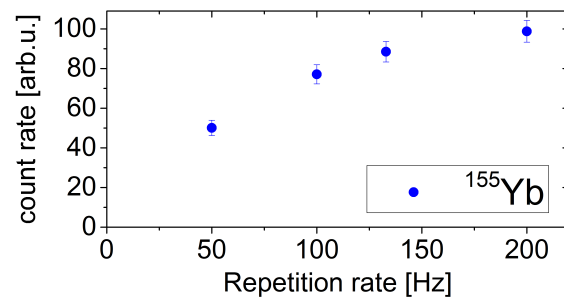

Figure 6: Measured signal strength in dependence of the laser repetition rate indicating a saturation at about 200 Hz, while at 100 Hz about 80% of the signal can be maintained.

can be used. Each dye laser provides laser pulses with an energy per pulse of at least 200 μJ and a pulse duration of about 18 ns. A third excimer laser (LPX220) is operated with a Xe:F gas mixture and the resulting laser radiation at 351 nm with pulse energies up to 150 mJ is used for the second (non resonant) ionization step for the wide range level search. The OPO is pumped by the third harmonic of a Nd:YAG laser at 355 nm and delivers laser pulses with energies as high as 2 mJ and wavelengths in the range from 205–700 nm depending on the settings and on the installed optical non-linear crystals. In contrast to the excimer lasers which operate at repetition rates of at least 100 Hz, the OPO system is limited to 50 Hz. This results in a loss in efficiency as shown in Fig. 6 where the measured count rate for ^{155}Yb is presented in dependence of the repetition rate of the laser system.

For resonant laser excitation and ionization, it is important to adjust the wavelength of the laser radiation as well as the spatial and temporal overlap of all laser pulses to ensure a high efficiency. The wavelengths of the four tunable dye laser radiations are measured in parallel using a commercial wavemeter (WS7, High Finesse) in combination with a fast four-channel fiber switch. The OPO laser radiation is monitored with a second wavemeter (LM007, ATOS). The interferometer patterns obtained from the wavemeter furthermore enables one to monitor the spectral quality of the laser radiation. This is of particular importance for fast degenerating UV dyes. To extend the effective lifetime of the dyes, the pump laser light is blocked every time the ions are accumulated onto the filament.

Since the lifetime of atomic levels may be very short (on the order of a few ns), it is crucial to guarantee a proper timing of the first excitation with respect to the second ionizing step. For synchronization, a pulse gen-

erator (Model 555, Berkeley Nucleonics Corporation) is used to trigger the pump lasers individually. The trigger signal for each excimer laser is fed into active synchronization units (LPA92, Lambda Physik). These stabilize the light output timing to a fixed delay using a feedback signal from a fast photodiode. The timing as well as the laser power is monitored with fast photodiodes inside the lasers and at the experimental place. Since all pump lasers are triggered from one pulse generator with a timing jitter below 1 ns, the remaining jitter of about 10 ns in the timing is dominated by intrinsic effects of the excimer lasers. For measurements with a delayed ionization, e.g. to determine the lifetime of an excited state, the time delay can be monitored. To this end, the time difference from the photodiode signal is converted by a time-to-analog-converter (TAC) in combination with an analog-to-digital converter (ADC).

The laser light of the dye lasers is transported for about 25 m from the laser laboratory to the experiment using individual multi-mode quartz fibers with a core diameter of 600 μm (LEONI Fiber Optics GmbH). For the coupling of the light into the fiber an anti-reflection(AR)-coated lens with a focal length of 38 mm is used. An overall transmission of 30–50% was achieved for wavelengths in the range of 300 to 430 nm. To optimize the spatial overlap of multiple fibers, a customized output coupler was designed. This coupling unit is an 80 mm long, cylindrical-shaped tool with four boreholes, which are slightly slanted with an angle of 1.5° to the optical axis. The fibers touch each other in a distance of 10 mm in front of the fiber coupler. Using a 2-inch collimation lens with a focal length of 75 mm parallel laser beams with diameters of 20 mm are achieved. An overlap of the laser beams emitted by the different fibers of more than 90% within the laser interaction region, located about 40 cm from the output coupler, was measured. The light of the ionizing laser is transported to the experimental setup by high reflective (HR) mirrors and is collimated using a lens of 10 m focal length. The measured transmission efficiency of the mirror system was about 45%. Before entering the cell, the laser beam is expanded in one direction using a cylindric telescope, that results in a beam profile of 25x35 mm^2 at the cell; large enough to ensure a full overlap with the laser beam of the first excitation step. Once the laser radiation has passed the gas cell, it is reflected back using a rectangular HR mirror to pass the cell a second time with a slight offset angle to enlarge the effective volume. This laser light is then retro reflected on the same beam path at about 3 m after the cell. In total, the laser light from the ionizing laser passes the gas cell four times.
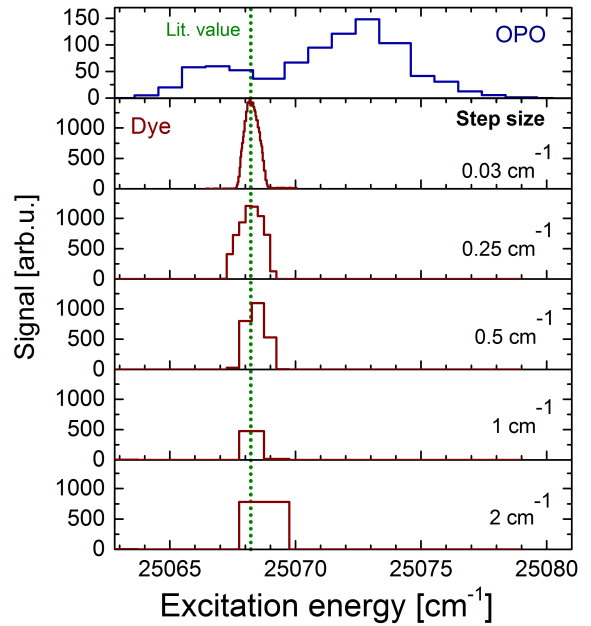

Figure 7: Laser scans exciting the 4f^{14}6s6p $^1P_1$ level in ytterbium for the OPO laser system and the dye laser system. The green dotted line shows the energy given for the transition in literature [22].

2.3. Scanning procedure

The effect of the scan step size for the search of atomic levels was investigated in a dedicated off-line gas cell using stable ytterbium isotopes where the level scheme is well known [22, 23]. Figure 7 shows the resonance signal obtained for different lasers and different step sizes. The resonant laser ionization was performed by tuning the light of a tunable laser to excite the 4f^{14}6s6p $^1P_1$ state at an excitation energy of 25 068.222 cm^{-1} corresponding to a vacuum wavelength of 398.9 nm. The atoms were then non-resonantly ionized by the laser radiation of an excimer laser at 351 nm. The upper spectrum in Fig. 7 shows the result obtained when the OPO laser was scanned across the wavenumber of the first excitation transition. A linewidth $\Delta\bar{\nu}_{\mathrm{FWHM}} = 5.4$ cm^{-1} can be deduced from the measurement. The shift of the resonance by 5 cm^{-1} is traced back to an intrinsic offset in the wavemeter readout (ATOS LM007). The accuracy was limited due to the wide bandwidth of the laser. The shoulder on the left end (see upper panel in Fig. 7) is attributed to a one-color two-photon excitation into a Rydberg level close to the first ionization potential at 50 443.2 cm^{-1}. The lower scans show the same res-
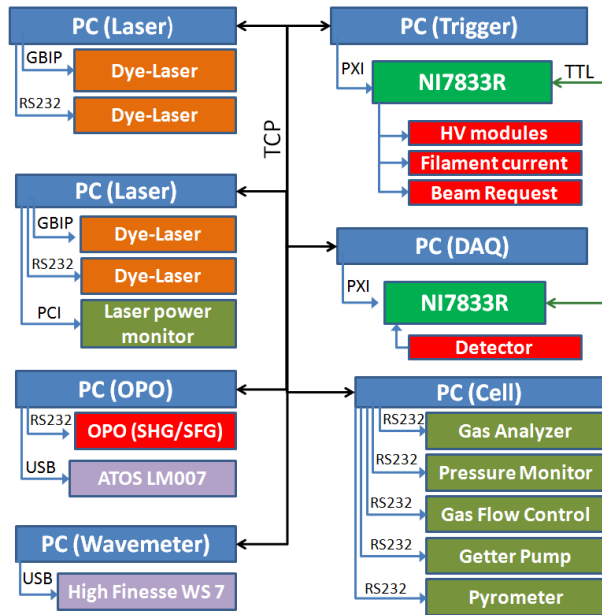
Figure 8: Block diagram of the DAQ and measurement control system.

Figure 9: Top: timing of the individual components during one measurement cycle optimized for ^{155}Yb. Bottom: detected ^{155}Yb alpha events (histogram) with respect to the cycle time. Here, the half-life of ^{155}Yb can be deduced from a best fit to the data (line).

onance obtained with a dye laser. A linewidth of $\Delta\bar{\nu}_{\mathrm{FWHM}} = 0.7\,\mathrm{cm}^{-1}$ was obtained when scanning the resonance with small steps of $0.03\,\mathrm{cm}^{-1}$. For the dye laser the wavelength was measured with a wavemeter (WS7, High Finesse) and the centroid of the resonance was located at $25\,068.256(4)\,\mathrm{cm}^{-1}$, obtained by fitting a Gaussian distribution to the data. The deviation of $0.034\,\mathrm{cm}^{-1}$ to the reported literature value [22] is comparable to the sampling interval. The lower graphs show the measured signal when increasing the spectral interval for each scan. From these measurements it can be deduced that the step size should not exceed $0.5\,\mathrm{cm}^{-1}$ to maintain a high efficiency while scanning.

2.3.1. Control system and data acquisition

The data acquisition (DAQ) and experiment control system has to handle a multitude of analog and digital signals simultaneously. The control and DAQ system includes controlling and monitoring the primary beam current, the laser system parameters as well as the vacuum components, ion optics, detectors, and the filament of the gas cell. These tasks are distributed among several computer systems in a local area network using TCP protocols, as depicted in Fig. 8. For the timing of the signals and the actual DAQ system two field-programmable gate array (FPGA) systems (National Instruments NI PXI 7833R) are available. These enable a real time synchronization of the digital triggers for
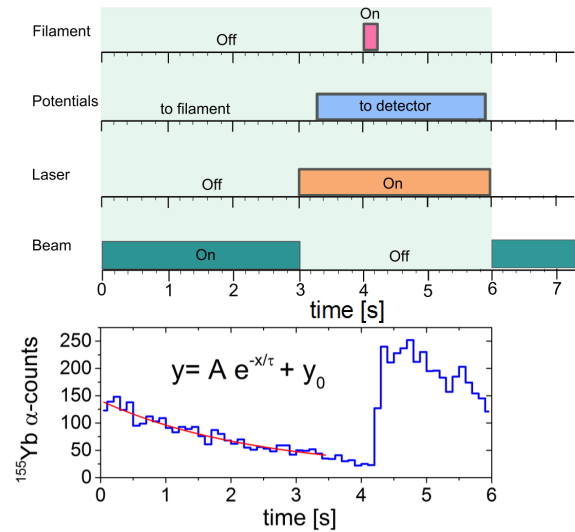
voltages, beam gates, and laser settings as well as for a proper time stamp to each registered signal. The system is controlled and read out by a LabView based DAQ software. The detector signals are handled on an event-by-event basis and are stored with all necessary information as the DAQ also receives data from all the measurement control computers. In addition, evaluated data files containing registered events with the wavelength information are stored for a fast on-line analysis.

A number of measurements were performed to test the speed and reliability of the DAQ system using a pulse generator. The dead time losses of the detection system were well below 0.5% until the signal rate approached 8 kHz after which the losses started to increase reaching about 2% at a signal rate of about 10 kHz. For comparison, the experimental α-rates for ^{155}Yb are well below 1 kHz while for ^{254}No less than only one event per second is expected.

3. Characterization using ytterbium

The measurements with the RADRIS method are performed in cycles whose optimum length strongly depends on the half-life of the isotope under investigation, as discussed in detail in [19, 9]. For testing and optimizing the entire setup the isotope ^{155}Yb ($T_{1/2} = 1.75\,\mathrm{s}$) was used. It was produced at SHIP in the
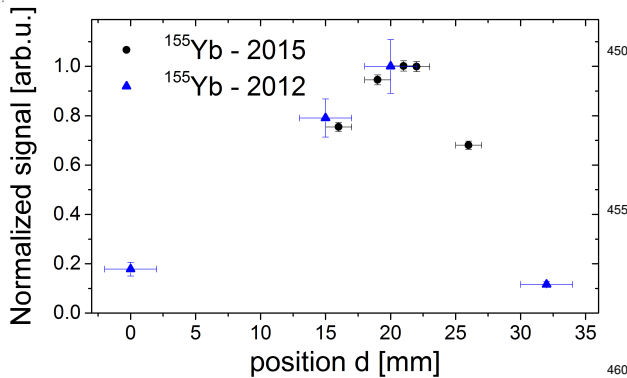
Figure 10: Dependence of the ^{155}Yb signal on the position of the filament obtained during two different beam times in 2012 an 2015. The uncertainty of the filament position is caused by the read-off accuracy.

fusion-evaporation reaction ^{112}Sn(^{48}Ca,5n)^{155}Yb with a cross section of about 7.5 mb.It was produced at SHIP in the fusion-evaporation reaction ^{112}Sn(^{48}Ca,5n)^{155}Yb with a beam energy of 4.55 A·MeV/u at which the products of the 6n(^{154}Yb) and 4n(^{156}Yb) evaporation channels contribute less than 30% to the recoil beam, but other evaporation residues such as ^{154}Tm (1p5n) are present with an intensity comparable to ^{155}Yb. The measurement cycle for ^{155}Yb is shown in the upper part of Fig. 9. Here, the ions were first neutralized and collected on the catcher filament for 3 s. Then the filament was heated for 0.3 s, evaporating the neutral ytterbium atoms which interact with the laser light. Laser induced ions were guided to the detector before a new cycle started. The laser pulse energies available at the experiment for resonant laser ionization were $E_1 = 160 \, \mu$J and $E_2 = 60$ mJ for the first and second step, respectively. The laser repetition rate was 100 Hz. The alpha decay from ^{155}Yb ($E_{155-\text{Yb}} = 5.199$ MeV) was detected. As the DAQ was permanently running, the cycle structure was imprinted on the detected signal as shown in the lower panel of Fig. 9. Here, the event-by-event handling and the according timestamps as well as the α-energies were used to evaluate the signal of ^{155}Yb with respect to the cycle duration. From the first 3 s of the cycle a half-life of $T_{1/2} = 1.64(40)$ s was deduced, which agrees well with the reported half-life of 1.75(5) s for ^{155}Yb [24]. The rise of the signal after a cycle time of 4 s coincides with the filament heating and indicates that the capturing and re-evaporation works.

3.1. Filament position

The optimization of the efficiency for catching and evaporating the stopped ions on the tip of the filament is important for the operation at lowest yields. Therefore, the filament position d (see Fig. 3) was varied and the signal of ^{155}Yb was measured. This measurement was performed in two different beamtimes. Fig. 10 shows normalized signal as a function of the filament position. At position $d = 0$ the tip of the filament is located at the center of the cell and has a distance of 68 mm from the entrance window. The signal shows a clear and reproducible maximum at $d = 20 - 22$ mm. The signal decreases rather rapidly for changes in the distance of about 5 mm in each direction away from the optimum which originates from two different effects - the stopping of the ions and the ion tranport to the detector.

To understand this behavior, simulations with the **S**topping and **R**ange of **I**ons in **M**atter (SRIM) [25] and SIMION [21] programs have been performed. Using the former theTo understand this behavior, simulations with the program **S**topping and **R**ange of **I**ons in **M**atter (SRIM) [25] have been performed. The stopping distribution was calculated for the specific experimental conditions, including the required degrader foils. For a recoil energy of 68 MeV in the case of ^{155}Yb, the mean stopping range of the evaporation residues amounts to $x_{Entr.} \approx 93$ mm behind the entrance window with a longitudinal distribution width of about 14 mm. If the filament is in the center position, the incoming ^{155}Yb ions are stopped behind the filament and cannot be efficiently captured on the tip of the filament. To have all ions stopped before the filament its position must be kept at $d \geq 15$ mm. A larger distance of $d \geq 25$ mm reduces the transport efficiency of laser induced ions towards the PIPS detectors, confirmed by ion optical simulations using SIMION. Within a position change of only 12 mm backwards, the efficiency drops by a factor of 8. Thus, the filament position is a crucial parameter that has to be carefully set.

3.2. Filament temperature

A second parameter that has to be optimized for the particular element under investigation is the filament temperature. Temperatures of at least 1350 K are required to efficiently evaporate nobelium from a tantalum filament, as determined in an earlier work by Laatiaoui et al [10]. The effect of higher evaporation temperatures on the laser ionization efficiency of ^{155}Yb was studied during a beamtime in 2015 (cf. Fig. 11). For these measurements the laser beam at the experiment had a diameter of about 20 mm and the temperature was measured with a fast optical pyrometer (LumaSense Tech., Impac IS 6 Advance).
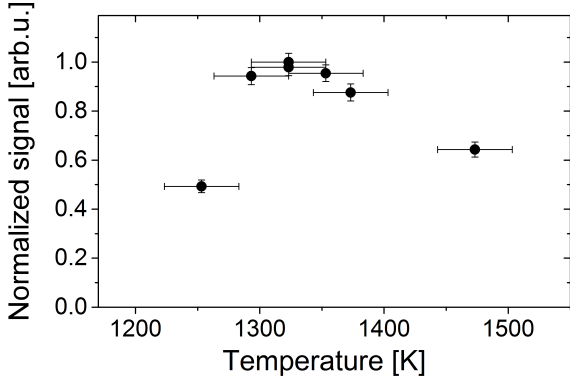
Figure 11: The normalized ^{155}Yb signal plotted as a function of the temperature of the filament.

Table 2: The calculated partial efficiencies in the RADRIS setup for ytterbium and nobelium. Comparing the product of all known contributions $\epsilon_{\text{estimate}}$ to the measured efficiency gives an estimate of the expected efficiency in ^{254}No, for details see text.

	^{155}Yb	^{254}No
ϵ_{in}	66%	76%
ϵ_{stop}	95%	100%
$\epsilon_{\text{collection}}$	37%	88%
ϵ_{decay}	51%	85%
$1 - \epsilon_{\text{neutr}}$	85%	93%
$\epsilon_{\text{detector}}$	40%	40%
$\epsilon_{\alpha\text{-branch}}$	89%	90%
$\epsilon_{\text{estimate}}$	**3.6%**	**19%**

For temperatures below about 1300 K ytterbium is not evaporated efficiently from the filament. For temperatures above 1400 K the efficiency decreases, which can be explained by increasing convection and diffusion effects. Off-line studies on the distribution of the Yb atoms for different heat loads support this interpretation of the data. Measurements during the beamtime in 2012 indicate that even for temperatures as high as 1850 K still reasonable efficiencies can be achieved. Unfortunately, the measurement conditions such as the laser beam size, gas pressure, and filament temperature were different and thus, the results cannot be compared directly. A stronger heating of the filament does not only reduce the filament lifetime, but also promotes a higher heat load into the stopping volume, leading to a fast spread of the vapor cloud above the filament. This in turn may result in a reduction of the efficiency.

3.3. Efficiency

The overall efficiency ϵ_{cell} is defined as the ratio of the detected α-event rate $\dot{n}^{\alpha}_{\text{Det}}$ to the ion rate measured before the gas cell $\dot{n}^{\text{ion}}_{\text{SHIP}}$

$$\epsilon_{\text{cell}} = \frac{\dot{n}^{\alpha}_{\text{Det}}}{\dot{n}^{\text{ion}}_{\text{SHIP}}} \quad . \tag{1}$$

The rate of ions entering the gas cell was determined using a 16-strip silicon detector with an active area of 80×35 mm^2 at the focal plane of SHIP. Due to the implantation depth of the high energetic recoils the detector efficiency for ^{155}Yb was calculated to $\epsilon^{155-\text{Yb}}_{\text{SHIP-Det}} = 0.71$ using the SRIM code, while for ^{254}No a value of $\epsilon^{254-\text{No}}_{\text{SHIP-Det}} = 0.55$ was calculated. To avoid radiation damage of the Si-detector and count rate losses due to pile-up or dead time of the data acquisition system, the

primary beam intensity was reduced to about 12 nA$_{\text{p}}$. In total 6080 ^{155}Yb ions per second arrived at the gas cell when scaling to a typical beam current of 300 nA$_{\text{p}}$ on the ^{112}Sn target taking into account the α-branching $\epsilon_{\alpha\text{-branch}} = 0.89$. The overall efficiency according to Eqn. 1 from the measured ^{155}Yb α-rate of $\dot{n}^{\alpha} = 80\,\text{s}^{-1}$ is $\epsilon_{\text{cell}} = 1.3(1)\%$.

As already discussed in [9], the cell efficiency can be factorized into different contributions

$$\epsilon_{\text{cell}} = \epsilon_{\text{in}} \times \epsilon_{\text{decay}} \times \epsilon_{\text{stop}} \times \epsilon_{\text{collection}} \times (1 - \epsilon_{\text{neutr.}})$$
$$\times \epsilon_{\text{detector}} \times \epsilon_{\alpha-\text{branch}} \times \epsilon_{\text{RIS}} \times \epsilon_{\text{evap}} . \tag{2}$$

Some of these partial efficiencies are different for ^{155}Yb and ^{254}No, as summarized in Tab. 2. Due to the differences in the geometric distribution of the incoming ions (c.f. distribution shown in Fig. 2) geometric acceptances for the entrance window setup of $\epsilon^{254-\text{No}}_{\text{in}} = 76\%$ and $\epsilon^{155-\text{Yb}}_{\text{in}} = 66\%$ are calculated for ^{254}No and ^{155}Yb, respectively. ~~The geometric distribution of the incoming ions is narrower in the case of ^{254}No, as can be seen in Fig. 2. This results in a higher transmission through the entrance window ϵ_{in}.~~ For ^{254}No (41 MeV) compared to ^{155}Yb (68 MeV) a better stopping efficiency ϵ_{stop} inside the gas cell is achieved with the existing setup. Additionally, for ^{155}Yb-ions a spatially larger distribution of the stopped ions is obtained. Simulations using SRIM and SIMION show that this influences the transport efficiency to the filament($\epsilon_{\text{collection}}$). Owing to the different half-lifes of ^{155}Yb and ^{254}No, different cycles were used, as discussed in [19]. Nevertheless, the efficiency that can be obtained during each cycle ϵ_{decay}

varies due to decay losses. The losses from neutralization of the stopped recoils ϵ_{neutr} are taken as 15% for ^{155}Yb, in accordance with ref. [9], while for ^{254}No a value for the neutralization of 7% was determined from direct transport of stopped ions to the detector. The detector efficiency $\epsilon_{\text{detector}}$ is the same in both cases and the α-branching is similar. The efficiencies for evaporation and resonance ionization as well as the losses by molecule formation cannot be easily calculated, but a combined value of 36% can be estimated comparing the measured efficiency of 1.3(1)% to the estimation of 3.6% from Tab. 2. Assuming the same efficiency for the evaporation and resonant laser ionization of nobelium, a total RADRIS efficiency of about 7% is expected for ^{254}No.

4. Summary and outlook

In the work reported upon the RADRIS setup was thoroughly optimized and characterized for resonant ionization of captured and evaporated fusion products. These experiments have been performed using ytterbium, the homologue of nobelium, which can be produced with higher rates. In these measurements, the filament position turned out to be a crucial parameter for the efficiency of the setup and an ideal configuration was found. Furthermore, the filament temperature should not exceed $1100\,°C$ (in the case of ^{155}Yb) to avoid losses from enhanced diffusion. The optimum laser step size for the level search in nobelium was determined to be $0.5\,\text{cm}^{-1}$. Taking into account the projected efficiency of 6.5% for nobelium and an incoming rate of four ions per second, about eight α-events are expected for resonant ionization in a 30 s cycle. In total 11 000 scan steps are required to cover the full range spanned by theoretical predictions, from $25\,000$–$31\,500\,\text{cm}^{-1}$. This is equivalent to a scan time of about 45 h beam time operating four dye lasers in parallel, not taking into account the time required for dye changes.

Acknowledgments

References

[1] H. Backe, W. Lauth, M. Block, M. Laatiaoui, Nuclear Physics A 944 (2015) 492–517. doi:10.1016/j.nuclphysa.2015.07.002.

[2] E. Eliav, S. Fritzsche, U. Kaldor, Nucl. Phys. A 944 (2015) 518–550. doi:10.1016/j.nuclphysa.2015.06.017.

[3] M. Schädel, D. Shaughnessy, The chemistry of superheavy elements, Springer, 2014.

[4] M. Schädel, Angewandte Chemie international edition 45 (2006) 368–401.

[5] T. Sato, M. Asai, A. Borschevsky, T. Stora, N. Sato, Y. Kaneya, K. Tsukada, C. E. Düllmann, K. Eberhardt, E. Eliav, et al., Nature 520 (2015) 209–211. doi:10.1038/nature14342.

[6] M. Sewtz, H. Backe, A. Dretzke, G. Kube, W. Lauth, P. Schwamb, K. Eberhardt, C. Grüning, P. Thörle, N. Trautmann, P. Kunz, J. Lassen, G. Passler, C. Z. Dong, S. Fritzsche, R. G. Haire, Phys. Rev. Lett. 90 (2003) 163002. doi:10.1103/PhysRevLett.90.163002.

[7] W. Lauth, H. Backe, M. Dahlinger, I. Klaft, P. Schwamb, G. Schwickert, N. Trautmann, U. Othmer, Phys. Rev. Lett. 68 (1992) 1675–1678. doi:10.1103/PhysRevLett.68.1675.

[8] H. Backe, M. Hies, H. Kunz, W. Lauth, O. Curtze, P. Schwamb, M. Sewtz, W. Theobald, R. Zahn, K. Eberhardt, N. Trautmann, D. Habs, R. Repnow, B. Fricke, Phys. Rev. Lett. 80 (1998) 920–923. doi:10.1103/PhysRevLett.80.920.

[9] H. Backe, P. Kunz, W. Lauth, A. Dretzke, R. Horn, T. Kolb, M. Laatiaoui, M. Sewtz, D. Ackermann, M. Block, F. Herfurth, F. P. Heßberger, S. Hofmann, R. Mann, Europ. Phys. J. D 45 (2007) 99–106. doi:10.1140/epjd/e2007-00198-1.

[10] M. Laatiaoui, H. Backe, M. Block, F.-P. Heßberger, P. Kunz, F. Lautenschläger, W. Lauth, M. Sewtz, T. Walther, Europ. Phys. J. D 68 (2014) 71. doi:10.1140/epjd/e2014-40617-6.

[11] S. Fritzsche, Europ. Phys. J. D 33 (2005) 15–21. doi:10.1140/epjd/e2005-00013-1.

[12] A. Borschevsky, E. Eliav, M. J. Vilkas, Y. Ishikawa, U. Kaldor, Phys. Rev. A 75 (2007) 042514. doi:10.1103/PhysRevA.75.042514.

[13] Y. Liu, R. Hutton, Y. Zou, Phys. Rev. A 76 (2007) 062503. doi:10.1103/PhysRevA.76.062503.

[14] V. A. Dzuba, M. S. Safronova, U. I. Safronova, Phys. Rev. A 90 (2014) 012504. doi:10.1103/PhysRevA.90.012504.

[15] G. Münzenberg, W. Faust, S. Hofmann, P. Armbruster, K. Güttner, H. Ewald, Nucl. Instrum. Meth. 161 (1979) 65 – 82. doi:10.1016/0029-554X(79)90362-8.

[16] R.-D. Herzberg, P. Greenlees, P. Butler, G. Jones, M. Venhart, I. Darby, S. Eeckhaudt, K. Eskola, T. Grahn, C. Gray-Jones, et al., Nature 442 (2006) 896–899. doi:10.1038/nature05069.

[17] M. Leino, H. Kankaanää, R.-D. Herzberg, A. Chewter, F. Heßberger, Y. Le Coz, F. Becker, P. Butler, J. Cocks, O. Dorvaux, K. Eskola, J. Gerl, P. Greenlees, K. Helariutta, M. Houry, G. Jones, P. Jones, R. Julin, S. Juutinen, H. Kettunen, T. Khoo, A. Kleinböhl, W. Korten, P. Kuusiniemi, R. Lucas, M. Muikku, P. Nieminen, R. Page, P. Rahkila, P. Reiter, A. Savelius, C. Schlegel, C. Theisen, W. Trzaska, H.-J. Wollersheim, Europ. Phys. J. A 6 (1999) 63–69. doi:10.1007/s100500050318.

[18] W. Reisdorf, Z. Phys. A 300 (1981) 227–238. doi:10.1007/BF01412298.

[19] M. Laatiaoui, H. Backe, M. Block, P. Chhetri, F. Lautenschläger, W. Lauth, T. Walther, Hyperfine Interactions 227 (2014) 69–75. doi:10.1007/s10751-013-0971-x.

[20] V. S. Letokhov, Laser Photoionization Spectroscopy, Academic Press Inc., 1987. ISBN-10: 0124443206.

[21] D. A. Dahl, International Journal of Mass Spectrometry 200 (2000) 3–25. doi:10.1016/S1387-3806(00)00305-5.

[22] A. Kramida, Y. Ralchenko, J. Reader, NIST ASD Team, Nist atomic spectra database (version 5.0), Online, 2012. Available at http://physics.nist.gov/asd, accessed 15.01.2016.

[23] W. Meggers, J. Tech, J. Res. Nat. Bureau Stand. 83 (1978) 13–

70. doi:10.6028/jres.083.003.

[24] K. S. Toth, K. S. Vierinen, M. O. Kortelahti, D. C. Sousa, J. M. Nitschke, P. A. Wilmarth, Phys. Rev. C 44 (1991) 1868–1877. doi:10.1103/PhysRevC.44.1868.

[25] J. F. Ziegler, Srim, Online, 2016. URL: www.srim.org.